Inorganic Chemistry

Article

pubs.acs.org/IC

Classical and Nonclassical Germanium Environments in High-Pressure $BaGe_5$

Rodrigo Castillo, Wilder Carrillo-Cabrera, Ulrich Schwarz,* and Yuri Grin

Max-Planck-Institut für Chemische Physik fester Stoffe, Nöthnitzer Straße 40, 01187 Dresden, Germany

Supporting Information

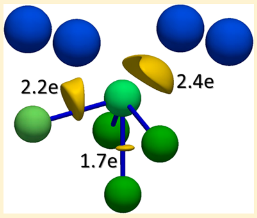

ABSTRACT: A new crystalline form of $BaGe_5$ was obtained at a pressure of 15(2) GPa in the temperature range from 1000(100) to 1200(120) K. Single-crystal electron and powder X-ray diffraction patterns indicate a body-centered orthorhombic structure (space group *Imma*, Pearson notation *oI*24) with unit cell parameters $a = 8.3421(8)$ Å, $b = 4.8728(5)$ Å, and $c = 13.7202(9)$ Å. The crystal structure of *hp*-$BaGe_5$ consists of four-bonded Ge atoms forming complex layers with Ge−Ge contacts between 2.560(6) and 2.684(3) Å; the Ba atoms are coordinated by 15 Ge neighbors in the range from 3.341(6) to 3.739(4) Å. Analysis of the chemical bonding using quantum chemical techniques in real space reveal charge transfer from the Ba cations to the anionic Ge species. Ge atoms having nearly tetrahedral environments show an electron-localizability-based oxidation number close to 0; the four-bonded Ge atoms with a Ψ-pyramidal environment adopt a value close to 1-. In agreement with the calculated electronic density of states, the compound is a metallic conductor (electrical resistivity of ca. 240 $\mu\Omega$ cm at 300 K), and magnetic susceptibility measurements evidence diamagnetic behavior with $\chi_0 = -95 \times 10^{-6}$ emu mol^{-1}.

INTRODUCTION

Intermetallic compounds attract ongoing interest in the field of basic materials science because of their promising thermoelectric or superconducting properties. Especially, cage compounds represent a promising novel class of potential materials, e.g., ternary clathrates of germanium and barium.[1] Aiming for the synthesis of potential materials in this class of compounds, the Ge-rich region of the binary Ba−Ge system was explored extensively. By the addition of high pressure as a synthesis parameter, access is granted to new framework patterns with occasional exceptional coordination numbers and interatomic distances of the network atoms (Figure 1). The achieved substantial modifications of the atomic environments often qualify the phases as favorable candidates for covalent metals with intriguing physical properties. Here, we report on the synthesis and characterization of a metallic high-pressure modification of barium pentagermanide, $BaGe_5$.

EXPERIMENTAL SECTION

Synthesis. All handlings were performed in gloveboxes [MBraun; $p(H_2O) \leq 0.1$ ppm and $p(O_2) \leq 0.1$ ppm]. The precursor samples with nominal composition Ba_6Ge_{25} were prepared by induction melting of a mixture of elemental Ba (Alfa Aesar, 99.98%) and Ge (Chempur, 99.9999%) in a sealed tantalum ampule to avoid mass losses. High-pressure conditions were realized with a Walker module employing MgO octahedra of 14 mm edge length. High temperatures were accomplished by resistive heating of graphite sleeves housing the *h*-BN crucibles. These enclosed stoichiometric mixtures (1:5) of the precursor Ba_6Ge_{25} and Ge (∼40 mg). The formation of *hp*-$BaGe_5$ was observed at a pressure of 15(2) GPa and in the temperature range from 1000(100) to 1200(120) K. The dwells at high-pressure conditions were carried out for 2 h, followed by quenching to ambient temperature before decompression. For a ratio of 1:6, $BaGe_5$ and Ge(*cF*8) were formed at 15 GPa and 1400 K.

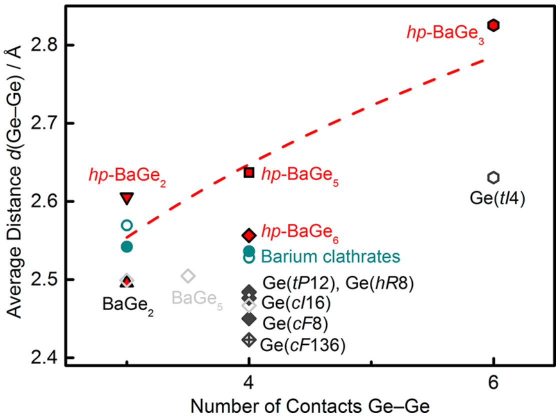

Figure 1. Number of Ge−Ge network contacts and average Ge−Ge distances in binary compounds of barium and germanium.[2−5] Please note that, e.g., for the high-pressure phase *hp*-$BaGe_3$, the number of framework contacts may exceed the connectivity of the Ge atoms, which is predicted on the basis of the Zintl concept and the 8 − *N* rule. The data for modifications of elementary Ge are shown for comparison.[6,7] The dashed curve shows an earlier observed scaling of the average Ge−Ge distances and the number of Ge−Ge contacts.[8]

Transmission Electron Microscopy (TEM) and Selected-Area Electron Diffraction (SAED) Tomography. The focused-ion-beam (FIB) technique was used for the preparation of thin cross sections of small crystalline particles. Defined crystallographic orientations of the layer-type compound were realized by using the cleavage plane (001) of *hp*-$BaGe_5$. Machined slices were prepared by a FIB technique using

Special Issue: To Honor the Memory of Prof. John D. Corbett

Received: September 30, 2014
Published: December 11, 2014

an FEI Quanta 200 3D dual-beam (SIM/SEM) device (FEI, Munich, Germany) equipped with an Omniprobe micromanipulator.

A piece of the bulk material was attached to a dedicated aluminum holder with conductive glue. With the cleavage surface on top, cuts were prepared parallel and perpendicular to the (001) plane, respectively (Figure 2a). A protective layer of platinum with thickness, height, and length of about 1.5, 2, and 20 μm, respectively, was deposited on the selected region using an accelerating voltage of 30 kV and a current of 0.1 nA. Each cross section (1.5 μm thickness) was prepared by applying a Ga-ion beam using an acceleration voltage of 30 kV and a current of 5−0.5 nA. The manufactured cut was transferred onto a copper Omniprobe TEM holder using the in situ lift-out technique.[9] Finally, the cross section was thinned to a thickness of about 60 nm by applying an acceleration voltage of 30 kV with currents of 1−0.01 nA of the Ga-ion beam.

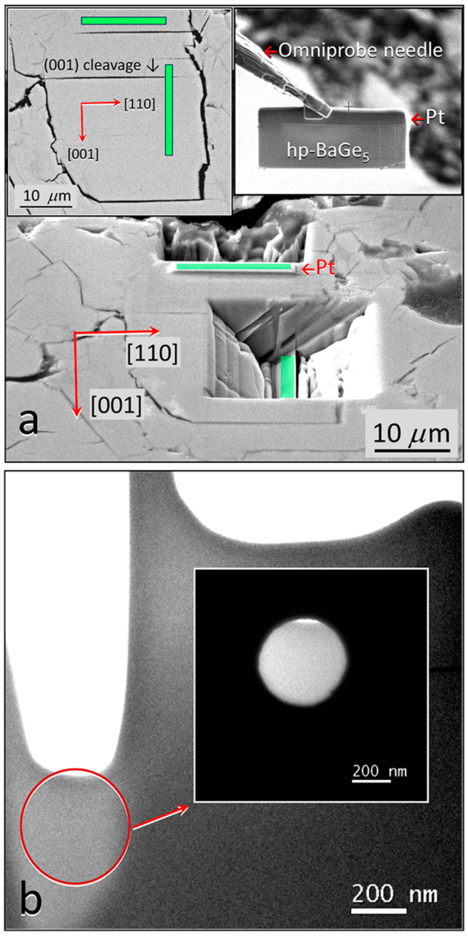

Figure 2. (a) SEM images of *hp*-BaGe$_5$ (polished sample) showing the positions of two oriented FIB cross sections (marked green) parallel and perpendicular to the (001) cleavage fracture, respectively. The top insets show the surface before the FIB experiment (left) and one lift-out cross section (right). (b) TEM image of the FIB cut showing the SAED region used for electron diffraction tomography. The inset shows the same region with the SAED aperture.

Conventional TEM and manually controlled diffraction tomography were performed on a FEI TECNAI 10 microscope (100 kV) equipped with a 2K CCD camera (TemCam-F224HD, TVIPS). The SAED mode was used for tomography data collection. A thin region of a crystal (slice perpendicular to a general direction; thickness of approximately 60 nm) was chosen for data acquisition. The selected area filled the full aperture with a diameter of about 440 nm (Figure 2b). Using a standard double-tilt holder (GATAN), a tilt sequence with a step width of 1° was performed in the range from −60° to +60°. The collected data were stored as files in TIF format and converted into MRC format stacks. Reconstruction of the diffraction volume was realized with the *ADT3D* software package.[10] After the spots were indexed in reciprocal space, the intensities were integrated and stored as a standard *hkl* file. A total of 582 reflections were measured and yielded 201 symmetry-independent observations.

Powder X-ray Diffraction. Phase identification was performed with a STOE-STADIP-MP diffractometer operating in Bragg−Brentano geometry (Ge monochromator, Cu Kα_1 radiation, λ = 1.54056 Å). Unit cell parameters were determined using 62 reflections (3° $\leq 2\theta \leq$ 120°; step width 0.02°, 3 × 10 h scans) of powder diffraction patterns measured with LaB$_6$ as an internal standard (a = 4.15692 Å). Least-squares refinements were carried out with the *WinXPOW* program.[11]

High-resolution powder X-ray diffraction data were collected on Beamline ID31 of the European Synchrotron Radiation Facility (ESRF) in Grenoble, France. A quartz capillary (Ø = 0.5 mm) was filled with the sample (particle size < 50 μm) and sealed in an argon atmosphere. The diffractometer was operated in Debye−Scherrer geometry (λ = 0.430459(5) Å; step width 0.001°; 1° $\leq 2\theta \leq$ 44°). Intensity recording was realized with a multianalyzer stage containing nine detectors, which were provided with Si(111) crystals. Rietveld refinement was performed using the crystallographic computing package *Jana 2006*.[12] Estimated standard deviations of the full profile refinements took into account local correlations of the powder diffraction data.[13] Details on data collection and structure refinement are summarized in Table 1.

Table 1. Crystallographic Data for *hp*-BaGe$_5$[a]

chemical formula	BaGe$_5$
space group	*Imma*
temperature/K	293(2)
a/Å	8.3421(8)
b/Å	4.8728(5)
c/Å	13.7202(9)
V/Å^3	557.72(9)
formula units Z	4
refinement	full profile
measured points, reflections	31000, 437
measured range, step/deg	3° $\leq 2\theta \leq$ 34°
h(min), k(min), l(min)	0, 0, 0
h(max), k(max), l(max)	11, 6, 18
$R(F)$, $R(wP)$	0.013, 0.06
GOF	0.76
refined parameters total, profile	35, 23

[a] Lattice parameters were refined using Cu Kα_1 radiation (λ = 1.54056 Å) with LaB$_6$ as an internal standard (62 reflections in the range 3° $\leq 2\theta \leq$ 120°). Powder X-ray diffraction patterns for refinement using full diffraction profiles were recorded with synchrotron radiation [λ = 0.430459(5) Å] at ID31 of ESRF using a nine-crystal multianalyzer stage and a step width of 0.001° for the summation.

Thermal and Chemical Analysis. Differential scanning calorimetry (DSC) experiments were performed using an Al$_2$O$_3$ crucible in a Netzsch DSC 404C apparatus (heating and cooling rate of 10 K min^{-1} from room temperature to 1300 K in an argon atmosphere). The peak onset temperatures were used for interpretation of the results.

Locally resolved chemical analysis was carried out on a polished sample for metallographic inspection using wavelength-dispersive X-ray spectroscopy (WDXS; Cameca SX 100) at 10 different points on the surface of the target phase.

Measurements of Physical Properties. For characterization of the magnetic susceptibility in external fields between 0.1 and 70 kOe, a SQUID MPMS XL-7 magnetometer (Quantum Design) was used for a bulk specimen of *hp*-BaGe$_5$ (7.46 mg) in the temperature range from 1.8 to 400 K. For electrical resistivity measurements with the standard alternating-current four-probe technique (PPMS, Quantum Design) in the temperature range from 2 to 350 K, a specimen with dimensions 0.74 × 0.80 × 1.10 mm^3 was employed. The inaccuracy of the electrical resistivity is estimated to amount to maximally ±40% because of uncertainties of the contact geometry.

Quantum Chemical Calculations. Electronic structure calculation and bonding analysis were carried out using the crystallographic data of *hp*-BaGe$_5$ (Tables 1 and 2). Density functional theory calculations with the Perdew–Wang/Ceperley–Alder[14] exchange-correlation functional were performed with the *Elk* code,[15] an implementation of the full-potential linearized augmented plane-wave method. The space was divided into muffin-tin and interstitial regions, in which atomic orbitals and plane waves were used as basis sets, respectively. The muffin-tin sphere radii were fixed to 2.2 bohr for Ba and 2.0 bohr for Ge, and the plane-wave cutoff of $|G + k|_{max} = 5.0/R_{mt}$ bohr^{-1} (R_{mt} = smallest muffin-tin radius) was chosen for the plane-wave expansion in the interstitial region. A mesh with 8 × 14 × 8 *k* points was used. For each self-consistent calculation, a basis set containing Ba(5s,5p,6d) and Ge(3p,4s,4p) as valence electrons was employed. Total energies were converged to less than 1 meV, and the difference in the effective potential was smaller than 0.1 meV between the final cycles.

Table 2. Atomic Coordinates and Isotropic Displacement Parameters for *hp*-BaGe$_5$

atom	Wyckoff position	*x*/*a*	*y*/*b*	*z*/*c*	U_{iso}/Å^2
Ba	4*e*	0	$^1/_4$	0.7826(3)	0.010(1)
Ge1	4*e*	0	$^1/_4$	0.0397(6)	0.010(2)
Ge2	8*i*	0.1534(5)	$^1/_4$	0.5576(3)	0.010(1)
Ge3	8*i*	0.2754(6)	$^1/_4$	0.1274(3)	0.009(1)

The electron localizability indicator (ELI, *γ*) was evaluated in the ELI-D representation[16] with an ELI-D module implemented in the *Elk* code. Topological analysis of the electron density, i.e., estimation of the shapes, volumes, and charges of the atoms, was done according to the Quantum Theory of Atoms in Molecules (QTAIM).[17] Topological analyses of the electron density and the ELI were performed with the program *DGrid*.[18]

RESULTS AND DISCUSSION

The synthesis of *hp*-BaGe$_5$ starts by mixing the precursors Ba$_6$Ge$_{25}$ and Ge at ambient pressure. The mixture of solid crystalline phases is thoroughly ground and subjected to a pressure of 15 GPa at temperatures between 1000 and 1200 K. WDXS measurements of the synthesized *hp*-BaGe$_5$ specimens indicate the composition $Ba_{0.9(1)}Ge_{5.1(1)}$, which corresponds within experimental uncertainty to the ratio Ba/Ge of 1:5.

The thermal behavior investigated by DSC measurement reveals three exothermic effects with temperatures starting at 469, 573.5, and 676.6 K on the heating curve (Figure 3). The first exothermic effect is assigned to a transition to a new, hitherto uncharacterized (metastable) phase with composition BaGe$_{5-x}$. Because this effect is irreversible and exothermic, *hp*-BaGe$_5$ is a metastable high-pressure phase. The second exothermic effect represents decomposition of BaGe$_{5-x}$ into a mixture of Ba$_8$Ge$_{43}$ and Ba$_6$Ge$_{25}$. Finally, the third exothermic effect indicates reaction of the clathrate mixture, yielding the ambient-pressure modification of BaGe$_5$. Upon further heating, the thermal behavior corresponds to that of the normal-pressure modification of BaGe$_5$ and consists of three endothermic effects occurring at 866, 1046, and 1082 K. The first signal is attributed to the transformation of BaGe$_5$ into Ba$_6$Ge$_{25}$ and Ge and the second one to the formation of Ba$_8$Ge$_{43}$. The third effect is assigned to the peritectic decomposition of Ba$_8$Ge$_{43}$ into Ge and the corresponding melt.[2] Figure 4 shows the powder X-ray diffraction patterns of the obtained phases after returning to room temperature.

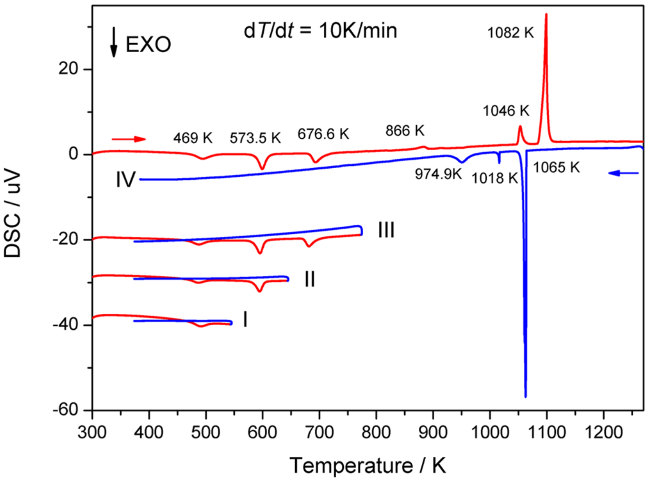

Figure 3. Thermal behavior of *hp*-BaGe$_5$ in different temperature ranges. Data in the direction of increasing temperatures are indicated in red; the results for cooling are shown in blue.

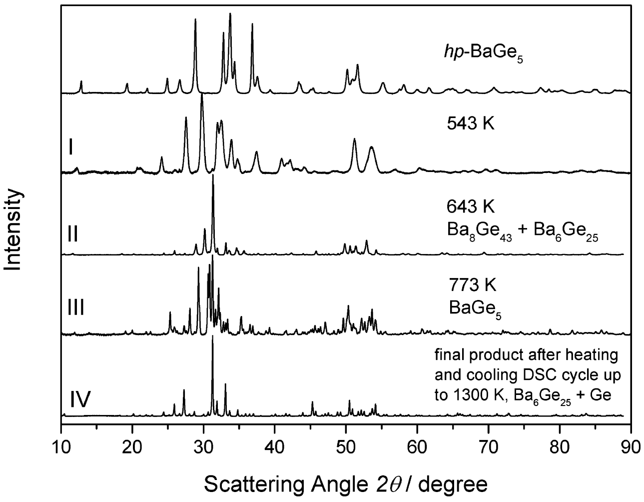

Figure 4. Powder X-ray diffraction patterns of *hp*-BaGe$_5$ and the products obtained after DSC measurements. The labeling (I–IV) corresponds to the conducted thermal cycles shown in Figure 3.

A first TEM experiment reveals diffuse diffraction patterns of the powdered particles indicating mechanical deformation of the crystallites. Therefore, three specimens for TEM studies have been prepared by FIB cutting. The electron diffraction tomography study suggests a body-centered orthorhombic structure with approximate lattice parameters *a* = 8.3 Å, *b* = 4.8 Å, *c* = 13.8 Å, and *α* = *β* = *γ* ≈ 90° (see Figure 5a–c), determined without symmetry restrictions.

Extinction conditions derived from the SAED patterns (Figure 5d–f) are in agreement with space groups *Imma*, *I*2*ma*, and *Im*2*a*: 0*kl*, *k* + *l* = 2*n*; *h*0*l*, *h* + *l* = 2*n*; *hk*0, *h*, *k* = 2*n*; *hkl*, *h* + *k* + *l* = 2*n*. The centrosymmetric space group *Imma* was chosen for crystal structure solution using the *SIR2011* program.[19] Refinement on the basis of the 3D electron diffraction intensity data of 201 symmetry independent reflections was realized with the *SHELXL* software.[20] The value for the residual *R* amounts to 0.31. Although seemingly

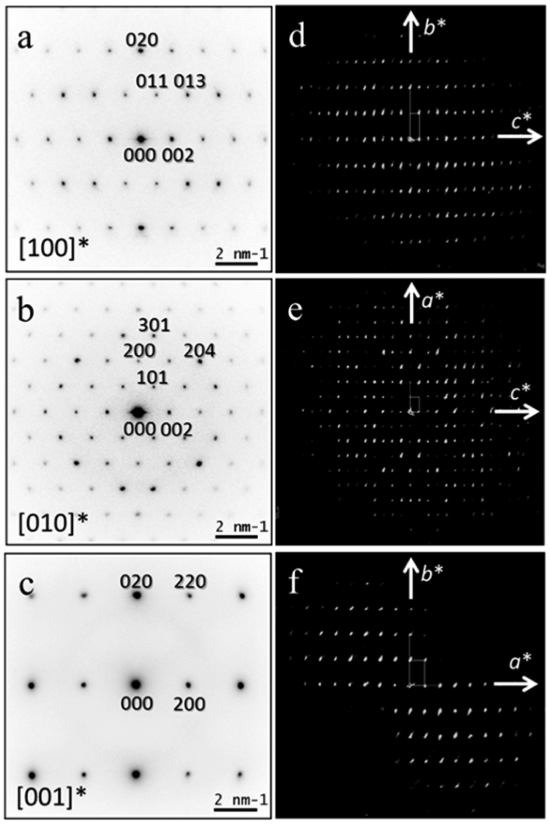

Figure 5. Electron diffraction on *hp*-$BaGe_5$: SAED images along the (a) [100]*, (b) [010]*, and (c) [001]* directions; projections of the 3D diffraction patterns (reciprocal volume) along the (d) [100]*, (e) [010]*, and (f) [001]* directions. 3D intensity data were used for crystal structure determination.

relatively high, such a value is normal for raw electron diffraction data.[10,21] The obtained structure model was refined using powder X-ray diffraction data measured with synchrotron radiation. The final lattice parameters, atomic coordinates, and isotropic displacement parameters are listed in Tables 1 and 2. Figure 6 illustrates refinement on the basis of powder X-ray diffraction data; the crystal structure is shown in Figure 7.

In the atomic pattern of *hp*-$BaGe_5$, 2D slabs of Ge atoms are separated by corrugated layers of the Ba atoms. The Ge layers contain six-membered rings in a boat conformation, with four Ge2 atoms forming the base and two Ge3 atoms shaping fore and aft. These rings are interconnected to double chains running along the [010] axis. Additional Ge1 zigzag chains are oriented in parallel. The condensation of these building units results in double layers perpendicular to [001] revealing a pronounced anisotropy of the crystal structure. Concerning the local configuration, all Ge atoms adopt four short Ge−Ge distances. Ge1 is coordinated in the form of a slightly distorted tetrahedron [$2d$(Ge1−Ge3) = 2.593(6) Å and $2d$(Ge1−Ge1) = 2.669(5) Å]. Ge2 shows also four short distances within a deformed tetrahedron [$1d$(Ge2−Ge2) = 2.560(6) Å + $1d$(Ge2−Ge3) = 2.608(6) Å + $2d$(Ge2−Ge3) = 2.684(3) Å] but with two additional longer distances [d(Ge2−Ge2) = 2.905(3) Å]. Finally, Ge3 forms an irregular coordination polyhedron derived from a Ψ pyramid [$1d$(Ge3−Ge1) = 2.593(6) Å + $1d$(Ge3−Ge2) = 2.608(6) Å + $2d$(Ge3−Ge2) = 2.684(3) Å]. The latter two atoms exhibit a pronounced similarity of the local environments to that of the framework atoms in β-$BaAl_2Ge_2$ (Al and Ge; Figure 7, bottom).[22]

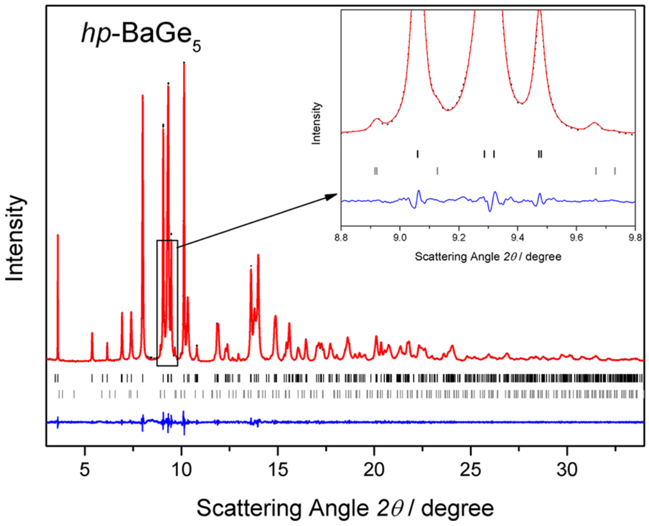

Figure 6. Synchrotron powder X-ray diffraction pattern of *hp*-$BaGe_5$. Reflection positions are marked by vertical ticks [black, *hp*-$BaGe_5$; gray, $BaGe_3$ (3 mass %, *hp*-$CaGe_3$-type crystal structure)]. The observed intensities are displayed as black points, and the calculated pattern is displayed as a red curve. The differences between the observed and calculated intensities are shown in blue. Selected reflections of the minority phase $BaGe_3$ are visualized in detail in the inset.

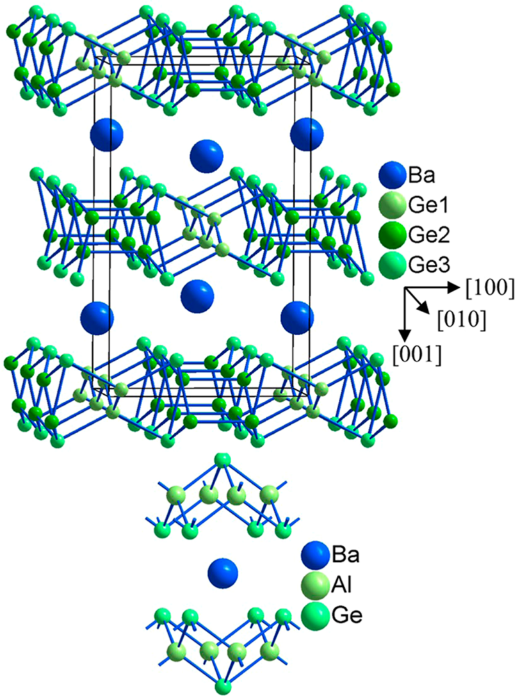

Figure 7. Crystal structure of *hp*-$BaGe_5$: (top) view along [010], with the four shortest distances of each Ge atom indicated by blue lines; (bottom) atomic arrangement of $BaAl_2Ge_2$ shown for comparison (see the text).[22]

Organization of the chemical bonding in *hp*-$BaGe_5$ is investigated by analysis of the atomic interactions in real space within the electron-localizability approach. Integration of the electron density within atomic basins, defined in accordance with the QTAIM technique,[17] yields effective charges amounting to Ge1$^{0.28-}$, Ge2$^{0.16-}$, Ge3$^{0.28-}$, and Ba$^{1.16+}$ (Figure 8). The charge on the Ge atoms averages to 0.24−. Assuming a complete transfer of the Ba valence electrons to the Ge substructure, a balance of $[\mathrm{Ba}^{2+}][\mathrm{Ge}^{0.4-}]_5$ would be expected. The finding of the experimental charges being significantly smaller than those calculated on the basis of the fully ionic balance indicates that charge transfer represents only part of the atomic interactions that are responsible for the bonding organization in *hp*-BaGe$_5$.

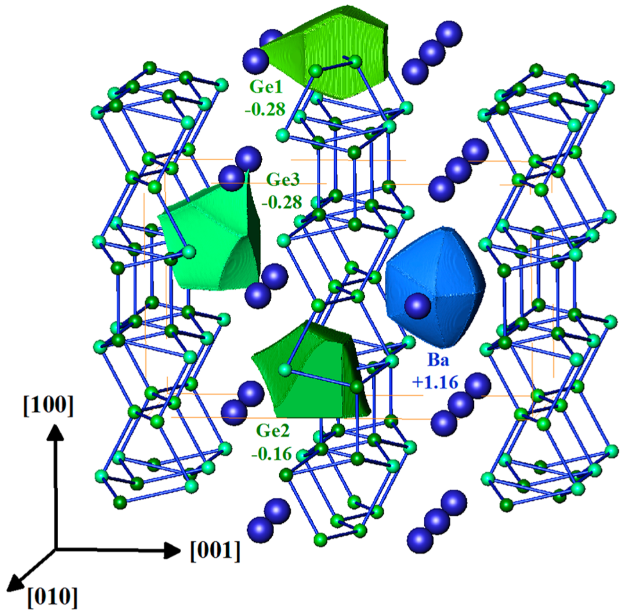

Figure 8. QTAIM atoms[17] and their effective charges in *hp*-BaGe$_5$.

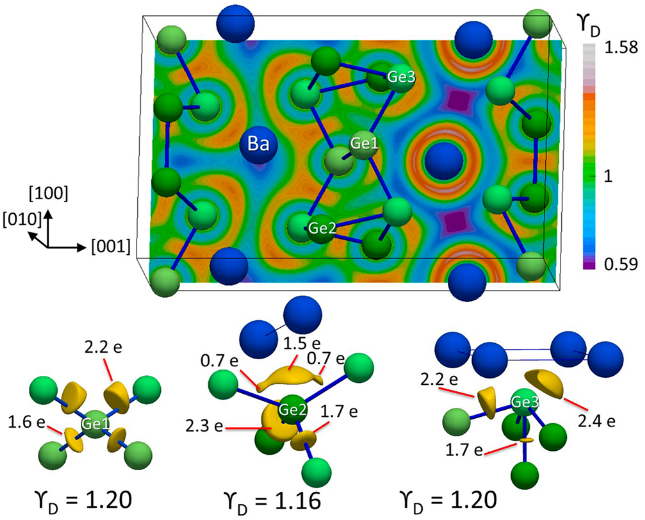

Figure 9. ELI-D in *hp*-BaGe$_5$. The shortest Ge−Ge distances (2.56−2.68 Å) are shown as blue lines. The ELI-D isosurfaces around Ge atoms visualize the positions of the attractors on the Ge−Ge bonds. For Ge2 and Ge3, selected neighboring Ba atoms are shown with short Ba−Ba distances indicated by thin lines.

According to the Zintl−Klemm concept and the 8 − *N* rule, a framework containing solely four-bonded tetrel atoms would not require additional electrons for stabilization. The *cF*136 modification of Ge exemplifies such an electron count.[7] Although containing large voids, the clathrate-II-type Ge framework $\square_{24}\mathrm{Ge}_{136}$ exists also without the filler atoms: $[(4b)\mathrm{Ge}^0]_{136}$ = $[(4b)\mathrm{Ge}^0]_8[(4b)\mathrm{Ge}^0]_{32}[(4b)\mathrm{Ge}^0]_{96}$. Binary clathrate-II-type frameworks may form defects in order to compensate for a surplus of electrons, at least partially. The emerging three-bonded network atoms are characterized by lone pairs involving a negative charge, e.g., in $\mathrm{Ba}_8\mathrm{Ge}_{43}$ = $[\mathrm{Ba}^{2+}]_8[(3b)\mathrm{Ge}^-]_{12}[(4b)\mathrm{Ge}^0]_{31}\square_3 \times 4e^-$ and $\mathrm{K}_8\mathrm{Ge}_{44}$ = $[\mathrm{K}^{1+}]_8[(3b)\mathrm{Ge}^-]_8[(4b)\mathrm{Ge}^0]_{36}\square_2$, respectively.[5,23] An alternative way is adopted in the ambient-pressure modification of BaGe$_5$ = $[\mathrm{Ba}^{2+}][(3b)\mathrm{Ge}^-]_2[(4b)\mathrm{Ge}^0]_3$ and in the clathrate $\mathrm{Ba}_6\mathrm{Ge}_{25}$ = $[\mathrm{Ba}^{2+}]_6[(3b)\mathrm{Ge}^-]_8[(4b)\mathrm{Ge}^0]_{17} \times 4e^-$. Here, part of the Ge atoms become three-bonded just by the topology of the framework without dedicated vacancy formation.[2,4] The modification of *hp*-BaGe$_5$ represents a third way to adapt a four-bonded Ge framework to the presence of excess electrons. This will be visualized by analysis of the ELI.

The distribution of ELI-D (Figure 9, top) in the vicinity of Ba shows a structuring in the fifth shell. This indicates participation of these electrons in the bonding interactions within the valence region. Furthermore, the ELI-D reveals maxima between the Ge atoms and their closest neighbors. Four maxima on the Ge1−Ge contacts confirm the four-bonded character, which has also been derived on the basis of the interatomic distances (Figure 9, bottom left). The ELI-D around Ge2 shows five attractors (Figure 9, bottom middle); four of them are located close to the Ge2−Ge contacts and have populations between 0.7 and 1.7 electrons. The fifth one is located within the quadrangle Ba−Ge3−Ge2−Ge3−Ba in the direction toward the second next-neighbor Ba, indicating a lone-pair-like multicenter interaction between Ge2 and Ba. Although the fifth shell of Ba is structured in the direction of this attractor (Figure 9, top), the lone-pair character of the interaction predominates because the basin of this attractor is by more than 95% located within the atomic basin of the Ge2 atom. This spatial organization is accompanied by enlargement of the Ge2−Ge3 distance to *d* = 2.684(3) Å. The ELI-D distribution around Ge3 (Figure 9, bottom right) has five maxima, four on the short Ge−Ge contacts or close to them and the fifth one, similarly to Ge2, in direction of the closest Ba atoms. This is taken as an indication for a lone-pair-like interaction in this region of the crystal structure. The lone-pair character is even more pronounced than that for Ge2 because the basin is located completely within the QTAIM basin of Ge3.

The disynaptic attractors on the Ge1−Ge contacts are well in agreement with four-bonded tetrel atoms. This is supported by the integration of the electron density in the bonding basin yielding 3.8 electrons per Ge1 atom. Consequently, the electron-localizability-based oxidation number[24] (ELIBON) amounts to 0.2+; i.e., it is close to Ge^0. These findings indicate two-center, two-electron bonds in this part of the crystal structure. Integrating the electron density within the bonding basins on the Ge2−Ge contacts yields 4.2 electrons per Ge atom and, thus, an ELIBON of 0.2−. The same operation for the Ge3−Ge contacts yields 5.05 electrons per Ge atom, i.e., an ELIBON of 1−. Hence, the atoms Ge1 and Ge2 with tetrahedron-like homoatomic coordination have electron counts close to that of Ge^0; the Ge3 atom with one lone pair corresponds roughly to Ge$^-$, yielding a complete electron balance of $[\mathrm{Ba}^{2+}][(4b)\mathrm{Ge1}^0][(4b)\mathrm{Ge2}^0]_2[\mathrm{Ge3}^-]_2$. This result indicates an electron-precise composition that is in agreement with the finding that the Fermi level is located in a pseudogap of the electronic density of states (DOS; Figure 10, bottom).

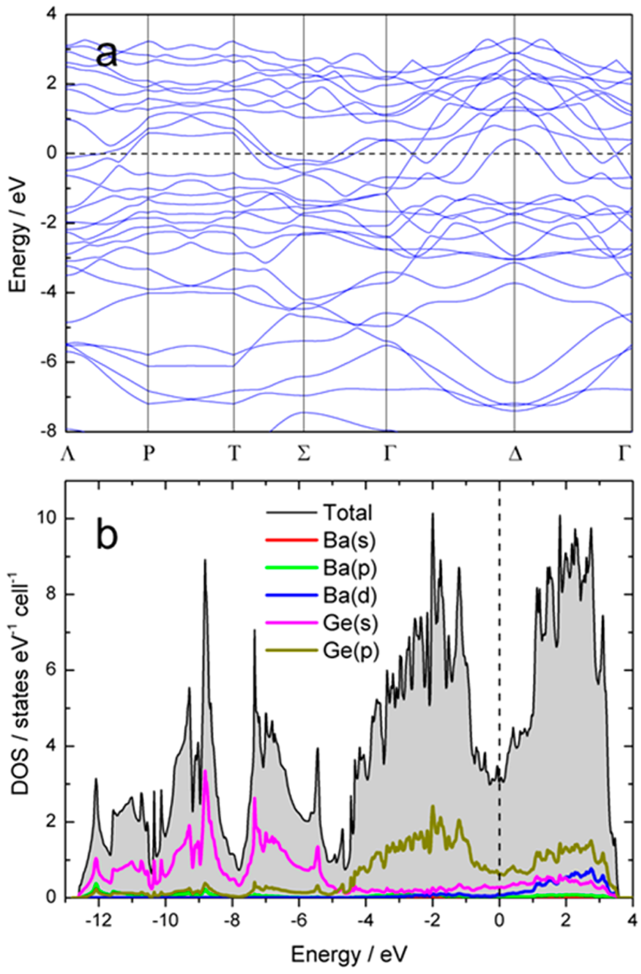

Figure 10. Electronic structure of *hp*-BaGe$_5$: (a) total band structure; (b) calculated total electronic DOS together with the orbital-resolved contributions.

Consistent with the findings of bonding analysis and the calculated band structure, the electrical resistivity of *hp*-BaGe$_5$ increases almost linearly with the temperature for $T > 50$ K. The data indicate metal-type electron-transport properties with a value of approximately 240 $\mu\Omega$ cm at 300 K and a residual resistivity of 15 $\mu\Omega$ cm at 4 K (Figure 11). The magnetic susceptibility is nearly independent of the temperature, showing diamagnetic behavior in the whole temperature range. The increase toward low temperatures is most likely caused by traces of paramagnetic impurities (Figure 11). The observed value of roughly 95×10^{-6} emu mol^{-1} at 300 K is in good agreement with the sum of the core diamagnetic contributions amounting to 110.5×10^{-6} emu mol^{-1}.

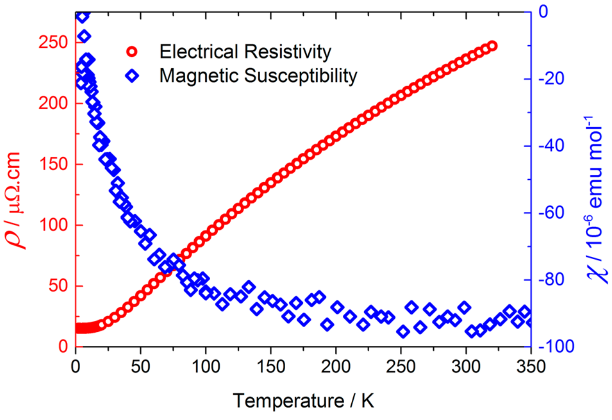

Figure 11. Electrical resistivity (red) and magnetic susceptibility measured at 70 kOe (blue) of *hp*-BeGe$_5$ as a function of the temperature.

In short, the new modification *hp*-BaGe$_5$ is synthesized at high-pressure high-temperature conditions. The crystal structure represents a new prototype for intermetallic compounds. The anionic part of the atomic arrangement consists of four-bonded Ge atoms, which are interconnected into 2D units. Chemical bonding analysis reveals additional lone-pair features at two of the three Ge atoms. The compound exhibits metal-type resistivity in accordance with the calculated electronic structure.

■ ASSOCIATED CONTENT

Ⓢ Supporting Information

Additional crystallographic information for *hp*-BaGe$_5$. This material is available free of charge via the Internet at http://pubs.acs.org.

■ AUTHOR INFORMATION

Corresponding Author

*E-mail: schwarz@cpfs.mpg.de.

Author Contributions

The manuscript was written through contributions of all authors. All authors have given approval to the final version of the manuscript.

Notes

The authors declare no competing financial interest.

■ ACKNOWLEDGMENTS

R.C. gratefully acknowledges the Becas Chile program for a doctoral grant. We thank Susann Leipe for high-pressure syntheses, Christina Drathen (ID31 at ESRF, Grenoble, France) and Yurii Prots for supporting synchrotron powder X-ray diffraction experiments, Marcus Schmidt and Susann Scharsach for DTA characterization, and Walter Schnelle and Ralf Koban for physical measurements.

■ REFERENCES

(1) (a) Zhang, H.; Borrmann, H.; Oeschler, N.; Candolfi, C.; Schnelle, W.; Schmidt, M.; Burkhardt, U.; Baitinger, M.; Zhao, J.-T.; Grin, Yu. *Inorg. Chem.* **2011**, *50*, 1250−1257. (b) Nguyen, L. T. K.; Aydemir, U.; Baitinger, M.; Bauer, E.; Borrmann, H.; Burkhardt, U.; Custers, J.; Haghighirad, A.; Hoefler, R.; Luther, K. D.; Ritter, F.; Assmus, W.; Grin, Yu.; Paschen, S. *Dalton Trans.* **2010**, *39*, 1071−1077. (c) Aydemir, U.; Candolfi, C.; Borrmann, H.; Baitinger, M.; Ormeci, A.; Carrillo-Cabrera, W.; Chubilleau, C.; Lenoir, B.; Dauscher, A.; Oeschler, N.; Steglich, F.; Grin, Yu. *Dalton Trans.* **2010**, *39*, 1078−1088. (d) Saramat, A.; Svensson, G.; Palmqvist, A. E. C.; Stiewe, C.; Mueller, E.; Platzek, D.; Williams, S. G. K.; Rowe, D. M.; Bryan, J. D.; Stucky, G. D. *J. Appl. Phys.* **2006**, *99*, 023708. (e) Alleno, E.; Lamquembe, N.; Cardoso-Gil, R.; Ikeda, M.; Widder, F.; Rouleau, O.; Godart, C.; Grin, Yu.; Paschen, S. *Phys. Status Solidi A* **2014**, *211*, 1293−1300.

(2) Aydemir, U.; Akselrud, L.; Carrillo-Cabrera, W.; Candolfi, C.; Oeschler, N.; Baitinger, M.; Steglich, F.; Grin, Yu. *J. Am. Chem. Soc.* **2010**, *132*, 10984−10985.

(3) (a) Evers, J.; Oehlinger, G.; Weiss, A. *Z. Naturforsch.* **1977**, *B32*, 1352−1353. (b) Evers, J.; Oehlinger, G.; Weiss, A. *Z. Naturforsch.* **1980**, *B35*, 397−398. (c) Fukuoka, H.; Tomomitsu, Y.; Inumaru, K.

Inorg. Chem. **2011**, *50*, 6372−6377. (d) Akselrud, L.; Wosylus, A.; Castillo, R.; Aydemir, U.; Prots, Yu.; Schnelle, W.; Grin, Yu.; Schwarz, U. *Inorg. Chem.*, DOI: 10.1021/ic5021065.

(4) (a) Carrillo-Cabrera, W.; Curda, J.; von Schnering, H. G.; Paschen, S.; Grin, Yu. *Z. Kristallogr. NCS* **2000**, *215*, 207−208. (b) Fukuoka, H.; Iwai, K.; Yamanaka, S.; Abe, H.; Yoza, K.; Häming, L. *J. Solid State Chem.* **2000**, *151*, 117−121. (c) Kim, S. J.; Hu, S.; Uher, C.; Hogan, T.; Huang, B.; Corbett, J. D.; Kanatzidis, M. D. *J. Solid State Chem.* **2000**, *153*, 321−329.

(5) Carrillo-Cabrera, W.; Budnyk, S.; Prots, Yu.; Grin, Yu. *Z. Anorg. Allg. Chem.* **2004**, *630*, 2267−2276.

(6) (a) Cooper, A. S. *Acta Crystallogr.* **1962**, *15*, 578−582. (b) Kasper, J. S.; Richards, S. M. *Acta Crystallogr.* **1964**, *17*, 752−755. (c) Nelmes, R. J.; McMahon, M. I.; Wright, N. G.; Allan, D. R.; Loveday, J. S. *Phys. Rev. B* **1993**, *48*, 9883−9886. (d) Schwarz, U.; Wosylus, A.; Boehme, B.; Baitinger, M.; Hanfland, M.; Grin, Yu. *Angew. Chem., Int. Ed.* **2008**, *47*, 6790−6793. (e) Wosylus, A.; Prots, Yu.; Schnelle, W.; Hanfland, M.; Schwarz, U. *Z. Naturforsch.* **2008**, *B63*, 608−614. (f) Ganguli, S.; Kazem, N.; Carter, D.; Kauzlarich, S. M. *J. Am. Chem. Soc.* **2014**, *136*, 1296−1299.

(7) Guloy, A. M.; Ramlau, R.; Tang, Z.; Schnelle, W.; Baitinger, M.; Grin, Yu. *Nature* **2006**, *443*, 320−323.

(8) Schnelle, W.; Ormeci, A.; Wosylus, A.; Meier, K.; Grin, Yu.; Schwarz, U. *Inorg. Chem.* **2012**, *51*, 5509−5511.

(9) Wang, Z.; Wan, W.; Sun, J.; Carrillo-Cabrera, W.; Grüner, D.; Yin, X.; Qiu, S.; Zhu, G.; Zou, X. *CrystEngComm* **2012**, *14*, 2204−2212.

(10) Kolb, U.; Mugnaioli, E.; Gorelik, T. E. *Cryst. Res. Technol.* **2011**, *46*, 542−554.

(11) *WinXPOW*, version 2.22; Stoe & Cie GmbH: Darmstadt, Germany, 2005.

(12) Petricek, V.; Dusek, M.; Palatinus, L. *Z. Kristallogr.* **2014**, *229*, 345−352.

(13) Berar, J.-F.; Lelann, P. *J. Appl. Crystallogr.* **1991**, *24*, 1−5.

(14) (a) Perdew, J.; Wang, Y. *Phys. Rev. B* **1992**, *45*, 13244−13249. (b) Ceperley, D. M.; Alder, B. J. *Phys. Rev. Lett.* **1980**, *45*, 566−569.

(15) *Elk*, version 1.4.18; http://elk.sourceforge.net; last accessed Nov 13, 2014.

(16) (a) Kohout, M. *Int. J. Quantum Chem.* **2004**, *97*, 651−658. (b) Wagner, F. R.; Bezugly, V.; Kohout, M.; Grin, Y. *Chem.—Eur. J.* **2007**, *13*, 5724−5741. (c) Kohout, M. *Faraday Discuss.* **2007**, *135*, 43−54. (d) Baranov, A. I.; Kohout, M. *J. Phys. Chem. Solids* **2010**, *71*, 1350−1356.

(17) Bader, R. F. W. *Atoms in Molecules: A Quantum Theory*; Clarendon Press: Oxford, U.K., 1990.

(18) Kohout, M. *DGrid*, version 4.6e; Max Planck Society: Radebeul, Germany, 2011.

(19) Burla, M. C.; Caliandro, R.; Camalli, M.; Carrozzini, B.; Cascarano, G. L.; Giacovazzo, C.; Mallamo, M.; Mazzone, A.; Polidori, G.; Spagna, R. *J. Appl. Crystallogr.* **2012**, *45*, 357−361.

(20) Sheldrick, G. M. *Acta Crystallogr., Sect. A* **2008**, *64*, 112−122.

(21) (a) Gemmi, M.; Galanis, A.; Karavassili, F.; Das, P. P.; Calamiotou, M.; Gantis, A.; Kollia, M.; Margiolaki, I.; Nicolopoulos, S. *Microsc. Micronal.* **2013**, *27*, 24−29. (b) Samuha, S.; Krimer, Y.; Meshi, L. *J. Appl. Crystallogr.* **2014**, *47*, 1032−1041.

(22) Leoni, S.; Carrillo-Cabrera, W.; Schnelle, W.; Grin, Yu. *Solid State Sci.* **2003**, *5*, 139−148.

(23) von Schnering, H. G.; Zürn, A.; Chang, J.-H.; Baitinger, M.; Grin, Yu. *Z. Anorg. Allg. Chem.* **2007**, *633*, 1147−1153.

(24) Veremchuk, I.; Mori, T.; Prots, Yu; Schnelle, W.; Leithe-Jasper, A.; Kohout, M.; Grin, Yu. *J. Solid State Chem.* **2008**, *181*, 1983−1991.